

# Maximizing the Lubricant Film Thickness Between a Rigid Microtextured and a Smooth Deformable Surface in Relative Motion, Using a Soft Elasto-Hydrodynamic Lubrication Model

Quentin Allen

Department of Mechanical Engineering,  
University of Utah,  
1495 E. 100 S. (1550 MEK),  
Salt Lake City, UT 84112  
e-mail: q.s.allen@utah.edu

Bart Raeymaekers<sup>1</sup>

Department of Mechanical Engineering,  
University of Utah,  
1495 E. 100 S. (1550 MEK),  
Salt Lake City, UT 84112  
e-mail: bart.raeymaekers@utah.edu

*We design a pattern of microtexture features to increase hydrodynamic pressure and lubricant film thickness in a hard-on-soft bearing. We use a soft elasto-hydrodynamic lubrication model to evaluate the effect of microtexture design parameters and bearing operating conditions on the resulting lubricant film thickness and find that the maximum lubricant film thickness occurs with a texture density between 10% and 40% and texture aspect ratio between 1% and 14%, depending on the bearing load and operating conditions. We show that these results are similar to those of hydrodynamic textured bearing problems because the lubricant film thickness is almost independent of the stiffness of the bearing surfaces in full-film lubrication. [DOI: 10.1115/1.4046291]*

*Keywords: surface texture, elasto-hydrodynamic lubrication, numerical analysis, film thickness, artificial joints, bio-tribology, elasto-hydrodynamic lubrication, surface treatments*

## 1 Introduction

Total hip replacement (THR) is one of the most common surgical procedures performed in the United States with over 326,000 surgeries performed in 2010 [1], and 572,000 projected to be performed annually by 2030 [2]. The success of this surgery in older populations is leading the trend for younger patients to undergo THR to relieve chronic joint pain [3]. A prosthetic hip joint consists of an acetabular component that is seated in the pelvis and a femoral head that is attached to a stem that is anchored in the femur (thigh) bone. The articulation between these components replaces the natural hip joint motion. Detailed figures and descriptions of prosthetic hip joint component geometry are widely available, see e.g., Ref. [4]. Different material pairs for prosthetic hip bearing surfaces exist in the marketplace, such as metal-on-polyethylene (MoP), metal-on-metal (MoM), ceramic-on-polyethylene (CoP), and ceramic-on-ceramic (CoC). Hard-on-soft material pairs have been employed since the beginning of THR [5] and are still the most common type due to their low-friction bearing surfaces, high fracture toughness, and documented clinical success [6,7]. Hard-on-hard material pairs were implemented to achieve lower wear rates [8] and have historically been popular for younger patients [9]; however, they can exhibit problems such as metal ion release [10,11] and squeaking [12,13]. Hard-on-soft bearings (especially CoP) continue to gain popularity, while hard-on-hard bearings are declining in common use [14]. In 2014, CoP bearings accounted for approximately 51% of new implants in the United States, MoP 42%, MoM 4%, and CoC 3% [15].

The longevity of prosthetic hip implants is often described by means of statistical survivorship, among other methods. It is well-known that the statistical survivorship of state-of-the-art prosthetic

hip implants decreases significantly after 15–20 years of use [16], depending on patient-specific parameters. With the average age of THR patients decreasing [3] and simultaneously, their life expectancy increasing, many patients are expected to outlive their prosthetic hip implant, thus requiring revision surgery during which a failed implant is replaced with a new one. The literature documents that MoP prosthetic hip implants fail primarily because of mechanical loosening (55%) and instability (14%) (which often result from osteolysis [17]), and osteolysis around a well-fixed implant (13%) [18]. Polyethylene wear debris originating from the articulation between the femoral head and the polyethylene acetabular liner plays a key role in each of these failure mechanisms.

Thus, reducing polyethylene wear remains of paramount importance to increase hip implant longevity of hard-on-soft prosthetic hip bearing material pairs. Researchers have attempted to reduce polyethylene wear by improving the mechanical properties and wear resistance of the polyethylene material, where notably the introduction of highly cross-linked polyethylene (HXPE) [19,20] and infusing/blending vitamin E into the HXPE [21] has significantly decreased both in-vitro and in-vivo wear [22]. Furthermore, ultra-smooth femoral head materials [23,24], surface coatings such as diamond-like carbon [25], tantalum [26], and titanium nitride [27,28], and adding a distinct surface texture to the bearing surfaces have also been implemented to reduce polyethylene wear. This manuscript specifically focuses on adding a deterministic microtexture to the hard bearing surface to reduce wear of the soft bearing surface in a hard-on-soft prosthetic hip implant material pair.

Several publications document that textured and microtextured bearing surfaces decrease friction and wear between hard-on-soft prosthetic hip implant bearing materials. Ito et al. used a hip simulator with a textured metal femoral head articulating against an ultra-high molecular weight polyethylene (UHMWPE) acetabular liner and measured a 16.9% and 69% reduction in the friction coefficient and polyethylene wear, respectively, which they attributed to the spherical texture features trapping wear debris and serving as lubricant reservoirs [29]. Several research groups have used

<sup>1</sup>Corresponding author.

Contributed by the Tribology Division of ASME for publication in the JOURNAL OF TRIBOLOGY. Manuscript received November 26, 2019; final manuscript received January 21, 2020; published online February 11, 2020. Assoc. Editor: Punit Kumar.

pin-on-disc (PoD) experiments to quantify the friction coefficient and wear between a textured metal disc and a polyethylene pin. Sawano et al. found a textured bearing to reduce polyethylene wear by 57% when compared with a smooth bearing and postulated that the texture features trap wear debris to reduce third-body abrasive wear [30]. Similarly, Cho and Choi documented that the friction coefficient of a textured bearing decreased by 68% when compared with a smooth one, as the texture changed the lubrication regime from boundary to (elasto)hydrodynamic lubrication [31]. Dougherty et al. observed similar results when texturing the polyethylene surface [32]. However, texturing the polyethylene surface ultimately leads to a changing texture geometry when it wears, which could alter the performance of the bearing. Other testing configurations including ball-on-disk [33] and ring-on-disk [34,35] have also been used to show that a deterministic surface texture reduces friction and polyethylene wear in a hard-on-soft bearing. It is important to point out that the aspect ratio of the texture features (defined as the ratio of texture depth to diameter) is large in all these experiments (aspect ratio > 10%), i.e., the primary function of the texture is to entrap and dispense lubricant, thus reducing friction and polyethylene wear. In contrast, Borjali et al. and Langhorn et al. used very shallow microtexture features (aspect ratio < 2%), designed to act as microhydrodynamic bearings that promote the formation of a lubricant film between the bearing surfaces. They performed uni-directional and multi-directional PoD experiments and found polyethylene wear to decrease by more than 50% when articulating with the microtextured when compared with the traditional smooth CoCrMo bearing surfaces, because the microtexture increases the lubricant film thickness, thus reducing contact, friction, and wear [36–38]. More complex wear experiments have also been performed; Chyr et al. used a hybrid device to show that microtexture on a cylindrical surrogate CoCrMo femoral head articulating with a polyethylene bearing surface reduces the friction coefficient up to 53% when compared with a smooth CoCrMo cylinder, by increasing hydrodynamic pressure and lubricant film thickness [39]. Choudhury et al. have used a high-speed camera and a pendulum hip simulator to visualize that the lubricant film thickness increases approximately 3.5 times with a microtextured when compared with a smooth bearing surface [40–42].

Numerical simulations have also been employed to study lubricant film thickness in hard-on-soft (textured) bearings. Particularly, different studies have focused on optimizing texture parameters including aspect ratio [43,44], diameter [45], density [46,47], and shape [48,49] to maximize lubricant film thickness or load-carrying capacity, minimize friction, or compute-bearing stiffness. Researchers have used computational fluid dynamics to solve the Navier–Stokes equations for lubricated rigid textured surfaces in two [50] and three [51] dimensions and found that load-carrying capacity increased and friction force decreased with increasing Reynolds number and increasing texture depth until the inception of vortex formation. Others have used numerical solutions of the Reynolds equation to describe lubricant flow in a rigid, microtextured bearing and find microtexture parameters that maximize lubricant film thickness and load-carrying capacity, while minimizing friction [39,49]. An elasto-hydrodynamic lubrication (EHL) model accounts for pressure-induced elastic deformation of the bearing surfaces by simultaneously solving the fluid film and elastic deformation equations. This method has been used to simulate lubricant pressure in, e.g., textured MoM prosthetic hip joints [45,52,53], where the metallic materials are conveniently modeled linear elastic. Soft EHL models cover conditions where the bearing surfaces deform at low pressure or when linear elasticity may not adequately model the material behavior [54]. Such models have been used to study, e.g., elastomeric seals [55] and lubrication of human skin [56] or eyelids [57]. Stupkiewicz et al. and Zhao et al. used finite element analysis (FEA) to simulate non-linear material models and complex geometries in soft EHL problems [58–60]. Shinkarenko et al. used a soft EHL model to describe the effects of material stiffness and microtexture geometry on load-carrying

capacity, mainly related to soft rubber materials for seals and gaskets [44,61,62]. Su et al. also used a soft EHL model to determine microtexture parameters that maximize the bearing load-carrying capacity in an MoP bearing [47]. Additionally, Qiu et al. computed the optimal microtexture parameters for a single-specific operating condition of a microtextured MoP knee implant bearing [63]. Several papers employ simulation to investigate textured and microtextured bearing surfaces, though most consider load-carrying capacity and not lubricant film thickness, and none cover the range of operating conditions present in a prosthetic hip joint.

No publications seem to exist that evaluate the effect of microtexture design parameters on the lubricant film thickness as a function of bearing operating parameters. The objective of this paper is to determine the effect of microtexture design parameters, material properties, and bearing operating conditions on the lubricant film thickness in microtextured hard-on-soft bearings, in the context of prosthetic hip implants, using a soft EHL computer model.

## 2 Methods

The model geometry comprises a rigid surface with an array of five concave spherical microtexture features, representing the microtextured surface of a femoral head, and a deformable counterface, representing the polyethylene acetabular liner. The undeformed surfaces are separated by nominal bearing spacing or clearance  $c$ , and the rigid surface slides parallel to the deformable surface with velocity  $U$ . At the small length scale considered here, the curvature of the femoral head and acetabular liner is negligible ( $\sim 1\%$ ) when compared with the length of the textured array. Likewise, the surface divergence due to a typical radial clearance and eccentricity of a femoral head/acetabular liner is very small ( $\sim 0.06$  deg at the worst case) and the surfaces are assumed to be parallel. An imaginary square cell of length  $2r_1$  surrounds each microtexture feature of depth  $h_p$  and radius  $r_p = 50 \mu\text{m}$ , which remains constant in this work. The microtexture geometry is fully described by its aspect ratio  $\varepsilon = h_p/2r_p$  and the texture density  $S_p = \pi r_p^2/4r_1^2$ . The local lubricant film thickness,  $h(x, y)$ , is the sum of the texture geometry, bearing spacing  $c$ , and polyethylene deformation,  $d(x, y)$ . Figure 1 shows a schematic of the model geometry.

We solve the two-dimensional (2D) steady-state, incompressible, iso-viscous Reynolds equation to compute the local lubricant film pressure:

$$\frac{\partial}{\partial x} \left( h^3 \frac{\partial p}{\partial x} \right) + \frac{\partial}{\partial y} \left( h^3 \frac{\partial p}{\partial y} \right) = 6\mu U \frac{\partial h}{\partial x} \quad (1)$$

where  $x$  and  $y$  refer to the Cartesian coordinate system defined in Fig. 1,  $h(x, y)$  is the local lubricant film thickness,  $p(x, y)$  is the local lubricant film pressure,  $\mu$  is the dynamic viscosity of the lubricant, and  $U$  is the relative velocity between both bearing surfaces. We non-dimensionalize Eq. (1) to render it independent of any specific lubrication system, using parameters similar to those used previously by our group as well as others [64]:  $P = p/p_0$ ,  $X = x/r_p$ ,  $Y = y/r_p$ , and  $H = h/c$ , where  $p_0$  is atmospheric pressure (101,325 Pa). Furthermore, we define a non-dimensional flow factor  $\lambda = 3\mu U/2r_p p_0$  and a non-dimensional nominal bearing spacing  $\delta = c/2r_p$ . Note that the flow factor incorporates the dynamic viscosity of the lubricant and relative sliding velocity between the bearing surfaces, thus describing the bearing operating conditions. Hence, the non-dimensional Reynolds equation yields:

$$\frac{\partial}{\partial X} \left( H^3 \frac{\partial P}{\partial X} \right) + \frac{\partial}{\partial Y} \left( H^3 \frac{\partial P}{\partial Y} \right) = \frac{\lambda}{\delta^2} \frac{\partial H}{\partial X} \quad (2)$$

We apply boundary conditions to simulate a geometrically repeating pattern of microtexture features, as it would be on a femoral head. We impose atmospheric pressure at the inlet ( $X = 0$ ) and outlet ( $X = 10r_1/r_p$ ) of the array of microtexture features. A single column of five microtexture features yields results free from edge effects, as the local lubricant film pressure becomes

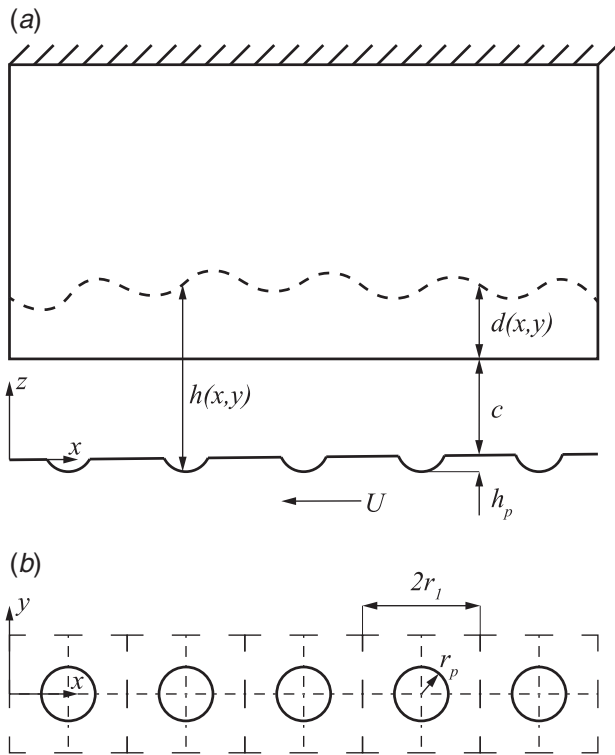


**Fig. 1 Schematic of the model geometry showing (a) a side view of the centerline of the rigid microtextured surface sliding with relative velocity  $U$  parallel to the deformable counterface. The dashed line schematically shows the deformation of the material and (b) a top view of the array of microtexture features on the rigid bearing surface, the dashed lines delineate the imaginary cells around the microtexture features.**

periodic in the  $x$ -direction after the second microtexture feature. We impose a symmetry boundary condition in the  $y$ -direction by requiring the first derivative of the lubricant film pressure with respect to the  $y$ -direction be zero at the edge ( $Y=r_t/r_p$ ) and center ( $Y=0$ ), which allows simulating only half of the column of microtexture features. We apply the Reynolds cavitation condition at each computation step to keep the lubricant film pressure from decreasing below the vapor pressure of water (5,630 Pa), which provides a conservative worst-case cavitation scenario when compared with simulations that use atmospheric pressure as the cavitation limit.

We employ a finite difference numerical method using central discretization to solve Eq. (2). Based on a convergence study with a grid of 301 by 301 nodes per imaginary cell, we determine that convergence occurs when the  $L2$ -norm of the difference between consecutive lubricant pressure solutions is less than  $10^{-3}$ . Improving the precision beyond  $10^{-3}$  changed the pressure result by less than 2% while significantly increasing the computation time. We implement a two-level multi-grid method to reduce the majority of the computation iterations to a grid with half as many nodes and perform two-dimensional linear interpolation between the grids, as described in Ref. [65]. The non-dimensional load-carrying capacity of the bearing is the integral of the pressure over the bearing area, or average non-dimensional lubricant film pressure,  $W = \iint P(X, Y) dXdY = P_{avg}$ .

We use FEA (ANSYS) to compute the deformation of a 3 mm thick section of polyethylene material (see Fig. 1), as if in the center of an acetabular liner. Thus, we rigidly constrain the top surface and apply the local lubricant film pressure computed from Eq. (2) to the polyethylene bearing surface as a gauge pressure load. Symmetry boundary conditions constrain lateral deflection of the inlet/outlet and side surfaces of the polyethylene counterface to model a small section from the bulk of the polyethylene acetabular liner.

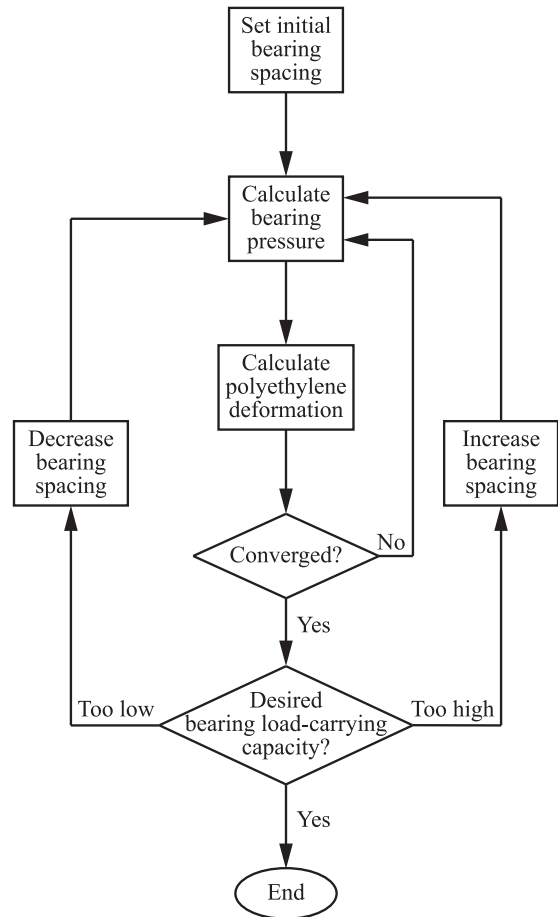


**Fig. 2 Flowchart illustrating the numerical simulations, involving simultaneous solution of the Reynolds equation (lubricant film pressure), the elastic deformation equations (deformation of the polyethylene material), and the external bearing load (load-carrying capacity)**

We do not consider the shear force from the fluid, as this would deform the polyethylene toward the bearing outlet, which would not alter the lubricant film thickness, but would result in unrealistic stress concentrations at the symmetry boundary conditions at the inlet and outlet of the model. Since this model is not free to rotate like, e.g., the models considered in Refs. [44,62], the influence of the shear force on the lubricant film thickness is negligible when compared with the normal pressure load. We use hexahedral brick-type elements with quadratic shape functions and six spatial degrees of freedom. A mesh convergence study shows that 20 elements across each imaginary unit cell, and 40 elements through the polyethylene depth yield a converged solution. Increasing the number of elements across each unit cell beyond 20 changed the deformation results by less than 0.50%, while increasing the number of elements through the depth beyond 40 changed the deformation results by less than 0.02%. We study the polyethylene deformation using a linear elastic constitutive model with Young's modulus  $E=0.9$  GPa and Poisson's ratio  $\nu=0.46$  [66], which we found to yield results identical to a J2 plasticity model [66], because the material does not plastically deform under the loading conditions considered here.

Figure 2 depicts a flow chart of the numerical simulation. We simultaneously solve the fluid film pressure problem (Eq. (2)) and the elastic deformation problem (FEA) by applying an external load to the bearing and an initial spacing between the bearing surfaces. We transfer data between both solutions with output text files from the pressure calculations becoming input for the FEA deformation calculation and vice versa. We iterate between pressure

and deformation until both equations simultaneously converge. Comparing the resulting bearing load-carrying capacity to the external bearing load then informs whether the bearing spacing needs to increase or decrease, after which the simulation restarts. The simulation ends when the lubricant film pressure and polyethylene deformation computation simultaneously converge and yield the desired bearing load-carrying capacity.

We have defined a range of design and operating parameters that span clinically relevant conditions for a prosthetic hip joint with a Newtonian lubricant. However, to maintain full-film lubrication, we consider flow factors higher than those experienced in the human hip by using an artificially high dynamic viscosity as adopted by others in similar simulations [67,68]. Table 1 lists the range of operating conditions and microtexture design parameters considered in this work, as well as the nominal values used for comparisons. ASTM F732 specifies the maximum contact stress of UHMWPE to be between 2 and 10 MPa during wear testing [69], while Saikko et al. recommend a constant-bearing load between 1 and 2 MPa for wear testing under static loading [70]. We evaluate bearing load-carrying capacities ranging between 0.25 and 2.00 MPa to be comparable with experimental data. We non-dimensionalize the bearing load-carrying capacity with atmospheric pressure (101,325 Pa), and the polyethylene stiffness  $K$  with the Young's modulus of polyethylene (0.9 GPa). We evaluate the texture density between its theoretical minimum ( $S_p=0$ ) and maximum ( $S_p=\pi/4$ ), and the texture aspect ratio between 0.01 and 0.10 to determine the optimum  $\varepsilon$  and  $S_p$  value that will

maximize the lubricant film thickness. We specifically determine the minimum lubricant film thickness  $H_{min}$  between the bearing surfaces because this is where contact first occurs. For clarity, we refer to the minimum lubricant film thickness that results from the optimum texture parameters ( $\varepsilon_{opt}$  and  $S_{p\ opt}$ ) as the optimum lubricant film thickness  $H_{opt}$ . Thus,  $H_{opt}$  represents the highest attainable minimum film thickness for a set of operating conditions (load-carrying capacity and flow factor).

### 3 Results and Discussion

**3.1 Typical Simulation Results.** Figure 3 shows an isometric view of the local lubricant film pressure and polyethylene deformation in a typical microtextured EHL bearing model simulated in this work. Inset images show a cross-sectional view of the lubricant film pressure, polyethylene deformation, and lubricant film thickness along the centerline of the bearing. From Fig. 3, we observe that the local lubricant film pressure decreases to the cavitation pressure limit as the lubricant fluid cavitates at the diverging edge of each microtexture feature and increases to its maximum value at the converging edge, similar to what has previously been reported by others [64]. Effects from adjacent texture features are accounted for by solving Eq. (2) over the entire domain at each computation step. The lubricant film pressure is almost periodic with respect to the microtexture features, except for the microtexture feature closest to the inlet and outlet, where effects from the atmospheric pressure boundary conditions occur. The periodic lubricant film pressure is also apparent in the polyethylene deformation as the locations of maximum and minimum pressure correspond to the maximum and minimum deformation of the polyethylene surface. Note the different scales of the axes of the inset images depicting the polyethylene deformation and lubricant film thickness. The lubricant film thickness is the sum of the nominal bearing spacing (before deformation) and the polyethylene deformation that results from the lubricant film pressure. We report the lubricant film thickness non-dimensionalized with the diameter of the texture features,  $H = h/2r_p$ , as this method preserves the trends of the dimensional values compared to the non-dimensionalization used for the numerical solution

**Table 1 Non-dimensional parameters**

Parameter	Minimum value	Maximum value	Nominal value
Load-carrying capacity, $W$	2.467	19.738	4.935
Flow factor, $\lambda$	0.003	0.300	0.300
Texture density, $S_p$	0.100	0.700	0.200
Texture aspect ratio, $\varepsilon$	0.010	0.100	0.050
Polyethylene stiffness, $K$	1	1000	1

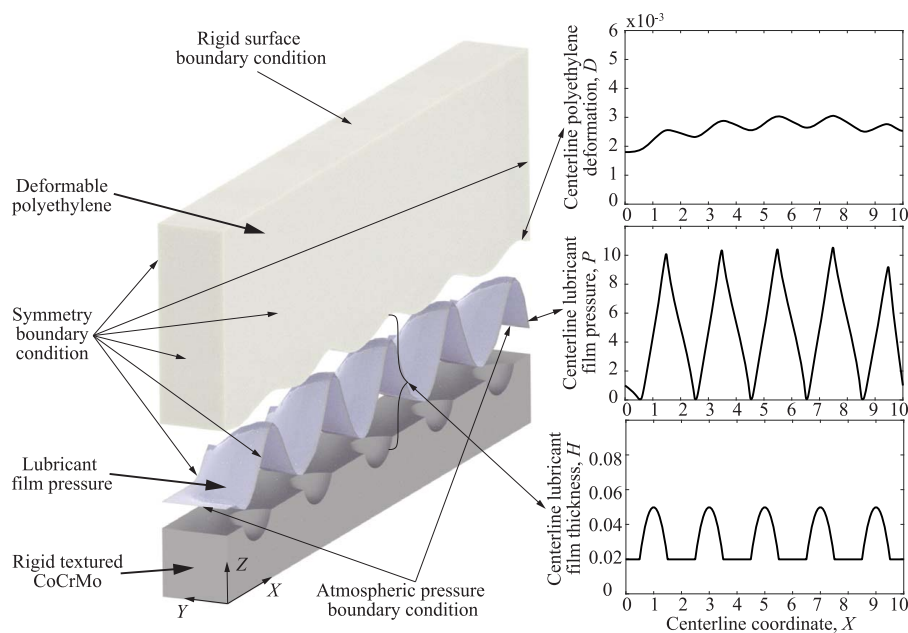


**Fig. 3 Schematic of a typical soft EHL solution ( $\varepsilon = 0.030$ ,  $S_p = 0.200$ ,  $\lambda = 0.030$ ,  $W = 4.935$ ) showing the lubricant film pressure across the microtexture array between the articulating surfaces. Note that the polyethylene deformation is exaggerated for clarity. Inset images show the local lubricant film pressure, polyethylene deformation, and lubricant film thickness along the centerline. The left side of the texture array ( $X = 0$ ) is the bearing inlet.**

of Eq. (2), which relies upon the bearing spacing  $c$  that changes with each simulation. The polyethylene deformation and bearing spacing are non-dimensionalized similarly:  $D(X, Y) = d(x, y)/2r_p$ ,  $\delta = c/2r_p$ .

**3.2 Effect of Bearing Operating Conditions on Lubricant Film Thickness.** We determine the microtexture geometry (texture aspect ratio and texture density) that maximizes the minimum lubricant film thickness as functions of flow factor and bearing load-carrying capacity. Figure 4(a) shows the minimum lubricant film thickness versus texture aspect ratio for select values of texture density and flow factor, whereas Fig. 4(b) shows the minimum lubricant film thickness versus texture aspect ratio for select values of texture density and bearing load-carrying capacity. We observe that the minimum lubricant film thickness reaches a maximum value for each bearing operating condition, i.e., the optimum lubricant film thickness  $H_{opt}$ . The texture parameters that lead to the maximum value of the minimum lubricant film thickness are also designated as optima, as described in Sec. 2. We also observe that near the optimum lubricant film thickness, multiple lines overlap, indicating that a range of texture density values around the optimum will result in similar minimum lubricant film thicknesses. Figure 5 shows the optimum lubricant film thickness as a function of (a) the flow factor and (b) the load-carrying capacity. The lubricant film thickness decreases with increasing bearing load-carrying capacity as expected and increases with increasing flow factor because the relative sliding velocity between the bearing surfaces and/or the lubricant dynamic viscosity increases with increasing flow factor. We use standard least-squares data fitting to determine power law best-fit equations (dashed lines in Fig. 5) that describe the optimum lubricant film thickness as a function of the flow factor, i.e.,  $H_{opt} = 0.136\lambda^{0.527}$  (with  $R^2 = 0.999$ ), and as a function of the load-carrying capacity, i.e.,  $H_{opt} = 0.182W^{-0.589}$  (with  $R^2 = 0.997$ ).

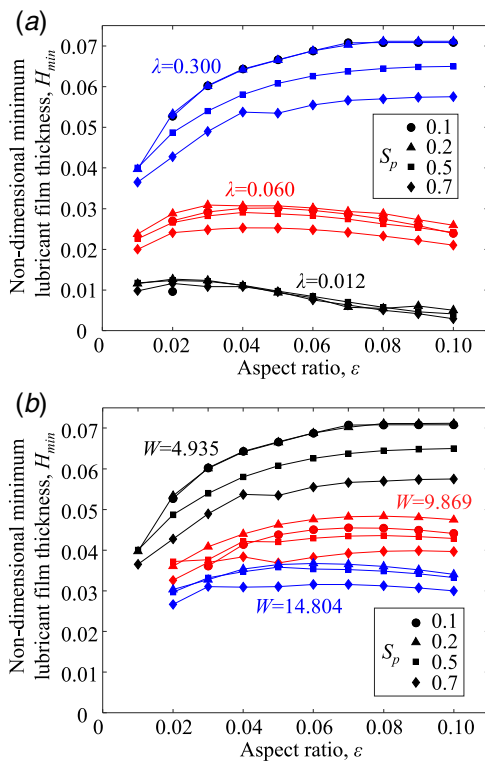


Fig. 4 Non-dimensional minimum lubricant film thickness as a function of texture aspect ratio for different values of texture density,  $S_p$ . (a) Showing flow factors of 0.012, 0.060, and 0.300, and (b) showing load-carrying capacities of 4.935, 9.869, and 14.804.

The lubricant film thickness is more sensitive to the texture aspect ratio than to the texture density because the former determines the capability of the texture feature to generate pressure, whereas the latter dictates how many texture features appear on the bearing surface. Figure 6 shows the optimum texture aspect ratio and optimum texture density as a function of (a) the flow factor and (b) the load-carrying capacity. The optimum texture density ranges between 0.10 and 0.40, depending on the flow factor and load-carrying capacity. A texture density in the range of 0.20–0.30 would result in a minimum lubricant film thickness near the highest possible value for almost every bearing operating condition we study, similar to what has been documented experimentally by others [31,34]. We also observe that the optimum texture aspect ratio varies between 0.01 and 0.14 depending on the flow factor and the bearing load-carrying capacity. The optimum texture aspect ratio increases with increasing flow factor and decreases with increasing load-carrying capacity, proportional with the optimum lubricant film thickness, as we will discuss in the next paragraph. A power law constitutes the best least-squares fit between the optimum texture aspect ratio and the flow factor, i.e.,  $\epsilon_{opt} = 0.172\lambda^{0.492}$  (with  $R^2 = 0.997$ ), and between the optimum texture aspect ratio and the load-carrying capacity, i.e.,  $\epsilon_{opt} = 0.214W^{-0.466}$  (with  $R^2 = 0.976$ ). These best-fit equations are superimposed on the data in Fig. 6 as dotted lines. Additionally, multiple regression analysis yields the least-squares best-fit equation for optimum texture aspect ratio as a function of both flow factor and bearing load-carrying capacity, i.e.,  $\epsilon_{opt} = 0.380\lambda^{0.511}W^{-0.445}$  (with  $R^2 = 0.992$  and a  $P$ -value of  $1.12 \times 10^{-11}$ ). Figure 7 shows contours of constant optimum texture aspect ratio determined from this expression as a function of flow factor and load-carrying capacity. Comparing the soft EHL simulation results to the experimental results obtained by Ma and Zhu [71] shows good qualitative agreement, as they demonstrate that the optimum texture aspect ratio (depth/diameter) increases with increasing velocity and decreasing bearing load. In the context of prosthetic hip joints, the soft EHL simulation results indicate that a lightweight, active patient (low load, high sliding velocity; top-left corner of Fig. 7)

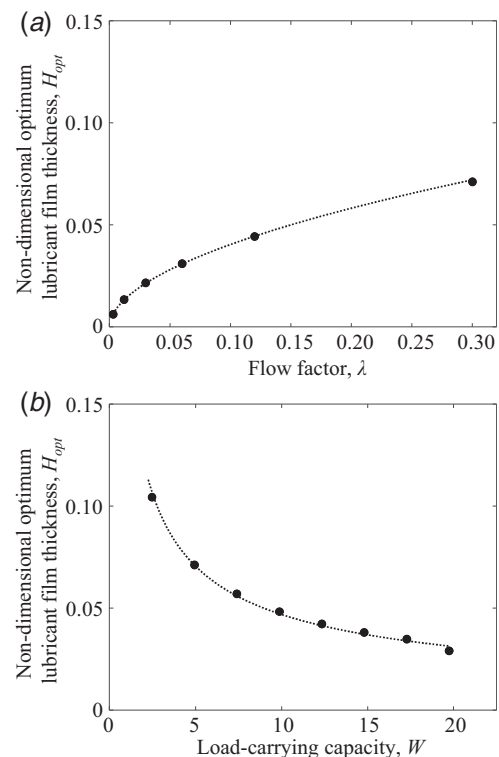
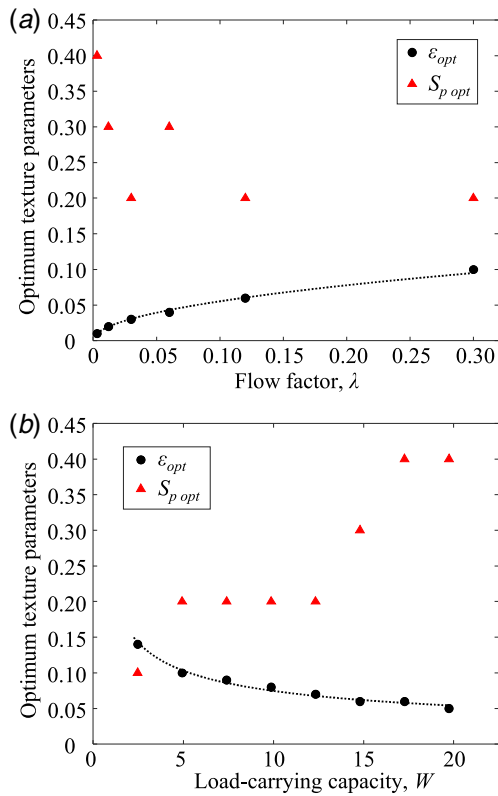
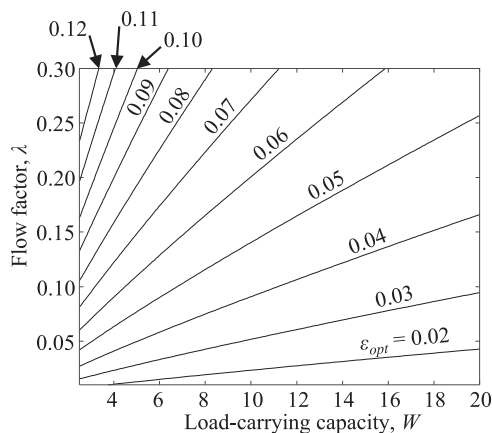


Fig. 5 Non-dimensional optimum lubricant film thickness as a function of (a) flow factor and (b) load-carrying capacity



**Fig. 6 Optimum texture parameters as a function of (a) flow factor and (b) load-carrying capacity. Dotted lines show the best-fit power law curves for the texture aspect ratio.**



**Fig. 7 Contours of constant optimum texture aspect ratio derived from multiple regression analysis**

would benefit from a femoral head textured with a higher texture aspect ratio than a heavy, inactive patient (high load, low sliding velocity; bottom-right corner of Fig. 7).

Why the optimum texture aspect ratio increases with increasing flow factor and decreases with increasing load-carrying capacity can be understood in terms of the optimum lubricant film thickness. The optimum texture aspect ratio is directly proportional to the optimum lubricant film thickness between the bearing surfaces, and both vary with the operating conditions. Codrignani et al. show a similar linear relationship between texture depth and gap height [72]. Figure 8 shows the optimum texture aspect ratio as a function of the optimum lubricant film thickness for a constant flow factor (triangle markers) and for a constant load-carrying

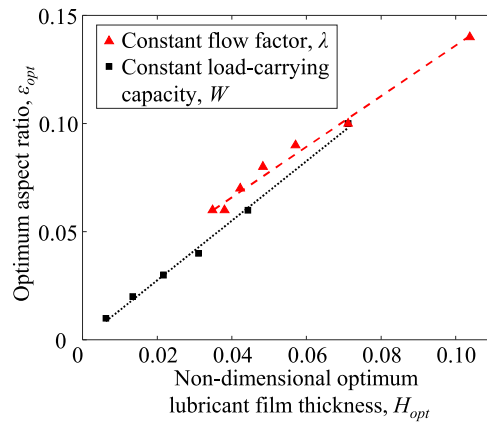


**Fig. 8 Optimum texture aspect ratio as a function of optimum lubricant film thickness**

capacity (circle markers). Both data sets display the same linearly increasing trend between optimum aspect ratio and optimum lubricant film thickness. The best least-squares linear fits are  $\epsilon_{opt} = 1.171H_{opt} + 0.019$  (dashed line,  $R^2 = 0.989$ ) and  $\epsilon_{opt} = 1.377H_{opt}$  (dotted line,  $R^2 = 0.997$ ), respectively. The optimum lubricant film thickness varies with flow factor and load-carrying capacity (average lubricant film pressure) according to a power law because of the nature of the Reynolds equation (Eq. (2)), i.e., a change in the lubricant film thickness ( $H$ ) results in non-linear changes of the other parameters ( $\lambda$ ,  $P$ ), which follow a power law (see best-fit equations in Fig. 5). Similar power law relationships describe the optimum texture aspect ratio as a function of the flow factor and bearing load-carrying capacity (see best-fit equations in Fig. 6). Therefore, a proportional relationship exists between the optimum texture aspect ratio and optimum lubricant film thickness.

**3.3 Effect of Material Properties on Bearing Stiffness.** The bearing stiffness,  $K_b$ , of a full-film lubricated bearing is the ratio of the change in load-carrying capacity and the corresponding change in minimum lubricant film thickness. Figure 9(a) shows the minimum lubricant film thickness as a function of the load-carrying capacity for a single, typical microtexture geometry ( $S_p = 0.20$ ,  $\epsilon = 0.05$ ) and flow factor ( $\lambda = 0.30$ ) for a range of linear elastic, non-dimensional polyethylene stiffness values ( $1 \leq K \leq 1000$ ) covering polymers ( $K = 1$ ), metals ( $K = 100$ ), and a rigid surface ( $K = 1000$ ). We observe that the bearing stiffness increases with decreasing lubricant film thickness, because the slope of  $W$  with respect to  $H_{min}$  increases with increasing  $W$ , similar to what others have documented [48]. The results of the different polyethylene stiffnesses overlap, indicating that the lubricant film thickness and bearing stiffness are both independent of the polyethylene stiffness for the range of parameters considered in this work. Figure 9(b) shows the nominal bearing spacing or undeformed clearance height  $\delta$ , and the corresponding minimum polyethylene deformation  $D_{min}$  for the range of polyethylene stiffness values. In a full-film lubrication model, the pressure generated in the lubricant film must balance the external bearing load (load-carrying capacity), regardless of the polyethylene material properties. Figure 9(b) illustrates that the minimum polyethylene deformation and nominal bearing spacing change inversely, adding up to the same minimum lubricant film thickness at each value of the load-carrying capacity independent of the polyethylene stiffness. If only the minimum lubricant film thickness or load-carrying capacity is of interest in a full-film lubrication bearing, the polyethylene deformation could be ignored. However, the deformation is important to gain an understanding of the behavior of the bearing materials, which ultimately affects wear.

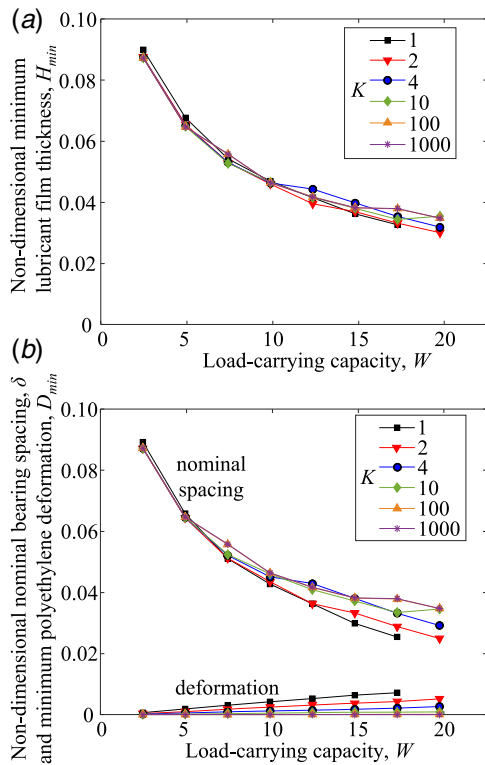


**Fig. 9** (a) Minimum lubricant film thickness as a function of load-carrying capacity, for different values of polyethylene stiffness,  $K$ . The bearing stiffness,  $K_b$ , is the slope defined by  $\Delta W/\Delta H_{min}$ . (b) Minimum lubricant film thickness separated into nominal bearing spacing and minimum polyethylene deformation. Note how the nominal bearing spacing and minimum polyethylene deformation add up to a similar minimum film thickness at each loading level, independent of the polyethylene stiffness.

In contrast to the polyethylene stiffness, changing the fluid lubricant properties (flow factor) does alter the bearing stiffness. Figure 10 shows the minimum lubricant film thickness as a function of load-carrying capacity for different values of the flow factor, for a typical microtextured bearing ( $S_p=0.2$ ,  $\varepsilon=0.05$ ) with constant polyethylene stiffness ( $K=1$ ). We observe that the minimum lubricant film thickness decreases and the bearing stiffness increases with decreasing flow factor. Least-squares best-fit curves of the minimum lubricant film thickness as a function of load-carrying capacity show a power law of the form  $H_{min}=aW^b$ , where  $a$  is a coefficient that determines the theoretical minimum lubricant film

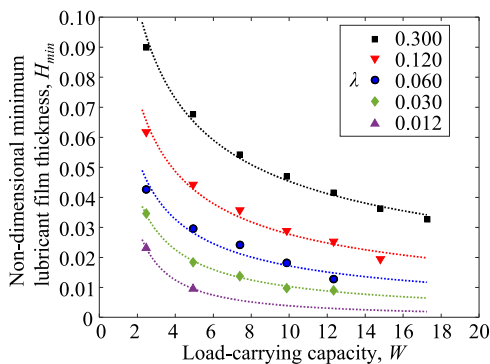


**Fig. 10** Minimum lubricant film thickness as a function of load-carrying capacity for different flow factors, illustrating bearing stiffness  $K_b = \Delta W/\Delta H_{min}$  as a function of flow factor

**Table 2** Coefficients and corresponding  $R^2$  values for the best-fit equations in Fig. 10

Flow factor	$a$	$b$	$R^2$
0.300	0.150	-0.519	0.991
0.120	0.114	-0.614	0.971
0.060	0.087	-0.703	0.942
0.030	0.074	-0.858	0.993
0.012	0.073	-1.279	1

thickness of an unloaded bearing ( $W=1$ ) and  $b$  is a decay exponent that describes how fast the minimum lubricant film thickness decreases with increasing load-carrying capacity. Table 2 shows the results for  $a$  and  $b$  as a function of each flow factor, along with the corresponding  $R^2$  values. In general,  $a$  decreases and  $b$  becomes increasingly negative with decreasing flow factor. This implies that the minimum lubricant film thickness decreases with decreasing flow factor, and more quickly approaches a terminal value with increasing load-carrying capacity. As a result, the bearing stiffness increases with decreasing flow factor and increasing load-carrying capacity. We also point out that the lubricant film pressure and load-carrying capacity must balance in each simulation. For a given load-carrying capacity, the lubricant film pressure remains constant, regardless of flow factor or lubricant film thickness. Since the polyethylene stiffness is constant in this round of simulations, the polyethylene deformation is similar for each value of the load-carrying capacity, independent of the flow factor.

**3.4 Accuracy.** The simulations in this work compute the lubricant film thickness of a microtextured hard-on-soft bearing, where no asperity contact occurs, i.e., the entire bearing load is carried by the lubricant film pressure. Typically, prosthetic hip joints operate under full-film lubrication during swing phase of the gait cycle, and in the boundary-mixed lubrication regime during stance phase of the gait cycle [73,74]. We perform the simulations with flow factors higher than those experienced in a prosthetic hip implant with normal in-vivo gait to ensure full-film lubrication for numerical simplicity and stability. Maximizing the lubricant film thickness during swing phase will allow the bearing to stay in the (elasto)hydrodynamic lubrication regime for a portion of the stance phase to reduce the fraction of the gait cycle that the bearing surfaces are in contact. Dougherty et al. found optimized textured surfaces to induce low-friction lubrication regimes at speeds that resulted in boundary lubrication for untextured surfaces [32]. All the limitations and assumptions inherent to the Reynolds equation apply to the results in this work. The EHL model does not always find a converged solution as the lubricant film thickness decreases, evidenced, e.g., by the missing data points in Fig. 10. We do not discuss friction in this work, because all simulations occur in the full-film lubrication regime where friction entirely results from fluid lubricant shear and increases with increasing flow factor, as shown experimentally [38]. Misalignments between femoral head and acetabular liner may also affect the results, as the effectiveness of surface texturing has been shown to decrease as the surfaces deviate from a parallel configuration [75]. Furthermore, we employ a simplified Newtonian lubricant and non mass-conserving cavitation model for computational simplicity and numerical stability. Accounting for realistic protein contributions to the bearing lubrication [76–79], shear-thinning lubricant behavior [74], or introducing a mass-conserving cavitation algorithm [80,81] would increase the accuracy of the results. Thermal effects can also have an effect on lubricant behavior [82–84], but were not considered here because a prosthetic hip implant operates at body temperature. The purpose of this paper is to determine optimum texture parameters by showing how the different texture designs perform relative to each other. A shear-thinning lubricant and/or mass-conserving cavitation model would result in more

accurate values of lubricant film pressure, but would likely apply a similar shift to the lubricant film thickness resulting from each microtexture design, resulting in a similar trend for optimum texture parameters as found with the simplified Newtonian lubricant and cavitation model used here. The simulation results are valid to identify optimum texture parameters for all microtextured hard-on-soft bearing pairs, including all MoP and CoP implants. Finally, we point out that some recent works [85,86] perform EHL computations with FEA/CFD in one software package, which contrasts the approach used in this work of a separate finite difference code and FEA software package to compute the lubricant pressure and polyethylene deformation, respectively. Since the lubrication problem in a prosthetic hip implant does not require the full Navier–Stokes equations, solving the Reynolds equation is computationally efficient, without compromising accuracy [43]. Furthermore, the shallow microtexture features used in this work make it difficult to obtain a high-quality FEA mesh, which affects accuracy.

## 4 Conclusions

We conclude that:

- (1) Optimum texture parameters exist for all hard-on-soft bearing operating conditions. For the conditions simulated here, the optimum texture density ranges between 0.10 and 0.40. Choosing a texture density in this range will help maximize the lubricant film thickness for a wide range of bearing operating conditions. The optimum texture aspect ratio increases by an order of magnitude from 0.01 to 0.14 with increasing flow factor and decreasing load-carrying capacity.
- (2) The optimum texture aspect ratio is proportional to the lubricant film thickness. Lubricant film thickness varies according to a power law with both flow factor and load-carrying capacity, which leads to a set of best-fit equations that enable predicting the optimum texture aspect ratio for given bearing operating conditions.
- (3) The flow factor, and not polyethylene stiffness, affects lubricant film thickness and bearing stiffness for any full-film lubrication bearing. The lubricant film thickness required to balance an external bearing load remains constant, independent of the polyethylene stiffness.

## Acknowledgment

We acknowledge support from the National Institutes of Health, National Institute of Arthritis and Musculoskeletal and Skin Diseases under grant 1R03AR066826-01A1.

## Nomenclature

$c$	= nominal bearing spacing, m
$E$	= Young's modulus, Pa
$K$	= non-dimensional polyethylene stiffness, $E/E_{UHMWPE}$
$U$	= relative sliding velocity between both bearing surfaces, m/s
$W$	= non-dimensional load-carrying capacity, $\iint P(X,Y)dXdY = P_{avg}$
$h_p$	= depth of texture feature, m
$p_0$	= atmospheric pressure, Pa
$r_1$	= half-length of imaginary square cell around each texture feature, m
$r_p$	= radius of texture feature, m
$D_{min}$	= minimum non-dimensional polyethylene deformation
$H_{min}$	= minimum non-dimensional lubricant film thickness
$H_{opt}$	= optimum non-dimensional lubricant film thickness
$S_p$	= texture density, $\pi r_p^2/4r_1^2$
$S_{p,opt}$	= optimum texture density
$x, y$	= Cartesian coordinates, m

$X, Y$	= non-dimensional Cartesian coordinate, $x/r_p, y/r_p$
$d(x, y)$	= polyethylene deformation, m
$h(x, y)$	= local lubricant film thickness, m
$p(x, y)$	= local lubricant film pressure, Pa
$D(X, Y)$	= non-dimensional polyethylene deformation, $d/2r_p$
$H(X, Y)$	= non-dimensional local lubricant film thickness, $h/c$ (simulation), or $h/2r_p$ (results)
$P(X, Y)$	= non-dimensional local lubricant film pressure, $p/p_0$
$\delta$	= non-dimensional nominal bearing spacing, $c/2r_p$
$\varepsilon$	= texture aspect ratio, $h_p/2r_p$
$\varepsilon_{opt}$	= optimum texture aspect ratio
$\lambda$	= flow factor, $3\mu U/2r_p p_0$
$\mu$	= dynamic viscosity, Pa·s
$\nu$	= Poisson's ratio

## References

- [1] Wolford, M. L., Palso, K., and Bercovitz, A., 2015, "Hospitalization for Total Hip Replacement Among Inpatients Aged 45 and Over: United States, 2000–2010," NCHS Data Brief, No. 186. National Center for Health Statistics, Hyattsville, MD.
- [2] Kurtz, S., Ong, K., Lau, E., Mowat, F., and Halpern, M., 2007, "Projections of Primary and Revision Hip and Knee Arthroplasty in the United States From 2005 to 2030," *J. Bone Jt. Surg.*, **89**(4), pp. 780–785.
- [3] Ravi, B., Croxford, R., Reichmann, W. M., Losina, E., Katz, J. N., and Hawker, G. A., 2012, "The Changing Demographics of Total Joint Arthroplasty Recipients in the United States and Ontario From 2001 to 2007," *Best Pract. Res. Clin. Rheumatol.*, **26**(5), pp. 637–647.
- [4] Foran, J. R. H., 2015, Total Hip Replacement, <https://orthoinfo.aaos.org/en/treatment/total-hip-replacement>, Accessed May 21, 2019.
- [5] Charnley, J., 1961, "Arthroplasty of the Hip," *Lancet*, **277**(7187), pp. 1129–1132.
- [6] Kurtz, S. M., 2004, *The UHMWPE Handbook: Ultra-High Molecular Weight Polyethylene in Total Joint Replacement*, Academic Press, Amsterdam.
- [7] Epinette, J. A., and Manley, M. T., 2014, "No Differences Found in Bearing Related Hip Survivorship at 10–12 Years Follow-Up Between Patients With Ceramic on Highly Cross-Linked Polyethylene Bearings Compared to Patients With Ceramic on Ceramic Bearings," *J. Arthroplasty*, **29**(7), pp. 1369–1372.
- [8] Zywiol, M. G., Sayeed, S. A., Johnson, A. J., Schmalzried, T. P., and Mont, M. A., 2011, "Survival of Hard-on-Hard Bearings in Total Hip Arthroplasty: A Systematic Review," *Clin. Orthop. Relat. Res.*, **469**(6), pp. 1536–1546.
- [9] Rajaei, S. S., Theriault, R. V., Pevear, M. E., and Smith, E. L., 2016, "National Trends in Primary Total Hip Arthroplasty in Extremely Young Patients: A Focus on Bearing Surface Usage From 2009 to 2012," *J. Arthroplasty*, **31**(9), pp. 63–68.
- [10] Vendittoli, P.-A., Mottard, S., Roy, A. G., Dupont, C., and Lavigne, M., 2007, "Chromium and Cobalt Ion Release Following the Durom High Carbon Content, Forged Metal-on-Metal Surface Replacement of the Hip," *J. Bone Jt. Surg.*, **89**(4), pp. 441–448.
- [11] Bosker, B. H., Ettema, H. B., Boomsma, M. F., Kollen, B. J., Maas, M., and Verheyen, C. C. P. M., 2012, "High Incidence of Pseudotumour Formation After Large-Diameter Metal-on-Metal Total Hip Replacement," *J. Bone Jt. Surg.*, **94-B**(6), pp. 755–761.
- [12] Owen, D. H., Russell, N. C., Smith, P. N., and Walter, W. L., 2014, "An Estimation of the Incidence of Squeaking and Revision Surgery for Squeaking in Ceramic-on-Ceramic Total Hip Replacement," *Bone Joint J.*, **96-B**(2), pp. 181–187.
- [13] Choi, I. Y., Kim, Y. S., Hwang, K. T., and Kim, Y. H., 2010, "Incidence and Factors Associated With Squeaking in Alumina-on-Alumina THA," *Clin. Orthop. Relat. Res.*, **468**(12), pp. 3234–3239.
- [14] Bedard, N. A., Burnett, R. A., DeMik, D. E., Gao, Y., Liu, S. S., and Callaghan, J. J., 2017, "Are Trends in Total Hip Arthroplasty Bearing Surface Continuing to Change? 2007–2015 Usage in a Large Database Cohort," *J. Arthroplasty*, **32**(12), pp. 3777–3781.
- [15] Heckmann, N. D., Sivasundaram, L., Steff, M. D., Kang, H. P., Basler, E. T., and Lieberman, J. R., 2018, "Total Hip Arthroplasty Bearing Surface Trends in the United States From 2007 to 2014: The Rise of Ceramic on Polyethylene," *J. Arthroplasty*, **33**(6), pp. 1757–1763.
- [16] Bayliss, L. E., Culliford, D., Monk, A. P., Glyn-Jones, S., Prieto-Alhambra, D., Judge, A., Cooper, C., Carr, A. J., Arden, N. K., Beard, D. J., and Price, A. J., 2017, "The Effect of Patient Age at Intervention on Risk of Implant Revision After Total Replacement of the Hip or Knee: A Population-Based Cohort Study," *Lancet*, **389**(10077), pp. 1424–1430.
- [17] Liu, A., Richards, L., Bladen, C. L., Ingham, E., Fisher, J., and Tipper, J. L., 2015, "The Biological Response to Nanometre-Sized Polymer Particles," *Acta Biomater.*, **23**, pp. 38–51.
- [18] Clohisy, J. C., Calvert, G., Tull, F., McDonald, D., and Maloney, W. J., 2004, "Reasons for Revision Hip Surgery: A Retrospective Review," *Clin. Orthop. Relat. Res.*, **429**, pp. 188–192.
- [19] Muratoglu, O. K., Bragdon, C. R., O'Connor, D. O., Jasty, M., and Harris, W. H., 2001, "A Novel Method of Cross-Linking Ultra-High-Molecular-Weight Polyethylene to Improve Wear, Reduce Oxidation, and Retain Mechanical Properties," *J. Arthroplasty*, **16**(2), pp. 149–160.
- [20] Laurent, M. P., Johnson, T. S., Crowninshield, R. D., Blanchard, C. R., Bhambri, S. K., and Yao, J. Q., 2008, "Characterization of a Highly Cross-Linked Ultrahigh

- Molecular-Weight Polyethylene in Clinical Use in Total Hip Arthroplasty," *J. Arthroplasty*, **23**(5), pp. 751–761.
- [21] Oral, E., Christensen, S. D., Malhi, A. S., Wannomae, K. K., and Muratoglu, O. K., 2006, "Wear Resistance and Mechanical Properties of Highly Cross-Linked, Ultrahigh-Molecular Weight Polyethylene Doped With Vitamin E," *J. Arthroplasty*, **21**(4), pp. 580–591.
- [22] Yamamoto, K., Tateiwa, T., and Takahashi, Y., 2017, "Vitamin E-Stabilized Highly Crosslinked Polyethylenes: The Role and Effectiveness in Total Hip Arthroplasty," *J. Orthop. Sci.*, **22**(3), pp. 384–390.
- [23] Saikko, V., 1994, "Wear of Polyethylene Acetabular Cups Against Zirconia Femoral Heads Studied With a Hip Joint Simulator," *Wear*, **176**(2), pp. 207–212.
- [24] Rahaman, M. N., Yao, A., Bal, B. S., Garino, J. P., and Ries, M. D., 2007, "Ceramics for Prosthetic Hip and Knee Joint Replacement," *J. Am. Ceram. Soc.*, **90**(7), pp. 1965–1988.
- [25] Brizuela, M., Garcia-Luis, A., Viviente, J. L., Braceras, I., and Oñate, J. I., 2002, "Tribological Study of Lubricious DLC Biocompatible Coatings," *J. Mater. Sci.: Mater. Med.*, **13**(12), pp. 1129–1133.
- [26] Balagna, C., Faga, M. G., and Spriano, S., 2012, "Tantalum-Based Multilayer Coating on Cobalt Alloys in Total Hip and Knee Replacement," *Mater. Sci. Eng. C*, **32**(4), pp. 887–895.
- [27] van Hove, R. P., Siersevelt, I. N., van Royen, B. J., and Nolte, P. A., 2015, "Titanium-Nitride Coating of Orthopaedic Implants: A Review of the Literature," *Biomed Res. Int.*, **2015**, pp. 1–9.
- [28] Ching, H. A., Choudhury, D., Nine, M. J., and Abu Osman, N. A., 2014, "Effects of Surface Coating on Reducing Friction and Wear of Orthopaedic Implants," *Sci. Technol. Adv. Mater.*, **15**(1), p. 014402.
- [29] Ito, H., Kaneda, K., Yuhta, T., Nishimura, I., Yasuda, K., and Matsuno, T., 2000, "Reduction of Polyethylene Wear by Concave Dimples on the Frictional Surface in Artificial Hip Joints," *J. Arthroplasty*, **15**(3), pp. 332–338.
- [30] Sawano, H., Warisawa, S., and Ishihara, S., 2009, "Study on Long Life of Artificial Joints by Investigating Optimal Sliding Surface Geometry for Improvement in Wear Resistance," *Precis. Eng.*, **33**(4), pp. 492–498.
- [31] Cho, M., and Choi, H.-J., 2014, "Optimization of Surface Texturing for Contact Between Steel and Ultrahigh Molecular Weight Polyethylene Under Boundary Lubrication," *Tribol. Lett.*, **56**(3), pp. 409–422.
- [32] Dougherty, P. S. M., Srivastava, G., Onler, R., Ozdoganlar, O. B., and Higgs, C. F., 2015, "Lubrication Enhancement for UHMWPE Sliding Contacts Through Surface Texturing," *Tribol. Trans.*, **58**(1), pp. 79–86.
- [33] López-Cervantes, A., Domínguez-López, I., Barceinas-Sánchez, J. D. O., and García-García, A. L., 2013, "Effects of Surface Texturing on the Performance of Biocompatible UHMWPE as a Bearing Material During in Vitro Lubricated Sliding/Rolling Motion," *J. Mech. Behav. Biomed. Mater.*, **20**, pp. 45–53.
- [34] Zhang, B., Huang, W., Wang, J., and Wang, X., 2013, "Comparison of the Effects of Surface Texture on the Surfaces of Steel and UHMWPE," *Tribol. Int.*, **65**, pp. 138–145.
- [35] Zhang, B., Huang, W., and Wang, X., 2012, "Biomimetic Surface Design for Ultrahigh Molecular Weight Polyethylene to Improve the Tribological Properties," *Proc. Inst. Mech. Eng. Part J J. Eng. Tribol.*, **226**(8), pp. 705–713.
- [36] Borjali, A., Langhorn, J., Monson, K., and Raeymaekers, B., 2017, "Using a Patterned Microtexture to Reduce Polyethylene Wear in Metal-on-Polyethylene Prosthetic Bearing Couples," *Wear*, **392–393**, pp. 77–83.
- [37] Langhorn, J., Borjali, A., Hippensteel, E., Nelson, W., and Raeymaekers, B., 2018, "Microtextured CoCrMo Alloy for Use in Metal-on-Polyethylene Prosthetic Joint Bearings: Multi-Directional Wear and Corrosion Measurements," *Tribol. Int.*, **124**, pp. 178–183.
- [38] Borjali, A., Monson, K., and Raeymaekers, B., 2018, "Friction Between a Polyethylene Pin and a Microtextured CoCrMo Disc, and Its Correlation to Polyethylene Wear, as a Function of Sliding Velocity and Contact Pressure, in the Context of Metal-on-Polyethylene Prosthetic Hip Implants," *Tribol. Int.*, **127**, pp. 568–574.
- [39] Chyr, A., Qiu, M., Speltz, J. W., Jacobsen, R. L., Sanders, A. P., and Raeymaekers, B., 2014, "A Patterned Microtexture to Reduce Friction and Increase Longevity of Prosthetic Hip Joints," *Wear*, **315**, pp. 51–57.
- [40] Choudhury, D., Vrbka, M., Mamat, A., Stavness, I., Roy, C. K., Mootanah, R., and Krupka, I., 2017, "The Impact of Surface and Geometry on Coefficient of Friction of Artificial Hip Joints," *J. Mech. Behav. Biomed. Mater.*, **72**, pp. 192–199.
- [41] Choudhury, D., Rebenda, D., Sasaki, S., Heikle, P., Vrbka, M., and Zou, M., 2018, "Enhanced Lubricant Film Formation Through Micro-Dimpled Hard-on-Hard Artificial Hip Joint: An in-Situ Observation of Dimple Shape Effects," *J. Mech. Behav. Biomed. Mater.*, **81**, pp. 120–129.
- [42] Choudhury, D., Urban, F., Vrbka, M., Hartl, M., and Krupka, I., 2015, "A Novel Tribological Study on DLC-Coated Micro-Dimpled Orthopedics Implant Interface," *J. Mech. Behav. Biomed. Mater.*, **45**, pp. 121–131.
- [43] Qiu, M., Bailey, B. N., Stoll, R., and Raeymaekers, B., 2014, "The Accuracy of the Compressible Reynolds Equation for Predicting the Local Pressure in Gas-Lubricated Textured Parallel Slider Bearings," *Tribol. Int.*, **72**, pp. 83–89.
- [44] Shinkarenko, A., Kligerman, Y., and Etsion, I., 2009, "The Effect of Surface Texturing in Soft Elastohydrodynamic Lubrication," *Tribol. Int.*, **42**, pp. 284–292.
- [45] Zhang, H., Hua, M., Dong, G. N., Zhang, D. Y., and Chin, K. S., 2016, "A Mixed Lubrication Model for Studying Tribological Behaviors of Surface Texturing," *Tribol. Int.*, **93**, pp. 583–592.
- [46] Wang, X., Wang, J., Zhang, B., and Huang, W., 2015, "Design Principles for the Area Density of Dimple Patterns," *Proc. Inst. Mech. Eng. Part J J. Eng. Tribol.*, **229**(4), pp. 538–546.
- [47] Su, B., Huang, L., Huang, W., and Wang, X., 2017, "The Load Carrying Capacity of Textured Sliding Bearings With Elastic Deformation," *Tribol. Int.*, **109**, pp. 86–96.
- [48] Qiu, M., Minson, B. R., and Raeymaekers, B., 2013, "The Effect of Texture Shape on the Friction Coefficient and Stiffness of Gas-Lubricated Parallel Slider Bearings," *Tribol. Int.*, **67**, pp. 278–288.
- [49] Zhang, Y. L., Zhang, X. G., and Matsoukas, G., 2015, "Numerical Study of Surface Texturing for Improving Tribological Properties of Ultra-High Molecular Weight Polyethylene," *Biosurf. Biotribol.*, **1**(4), pp. 270–277.
- [50] Sahlin, F., Glavatskih, S. B., Almqvist, T., and Larsson, R., 2005, "Two-Dimensional CFD-Analysis of Micro-Patterned Surfaces in Hydrodynamic Lubrication," *ASME J. Tribol.*, **127**(1), pp. 96–102.
- [51] Han, J., Fang, L., Sun, J., and Ge, S., 2010, "Hydrodynamic Lubrication of Microimprint Textured Surface Using Three-Dimensional CFD," *Tribol. Trans.*, **53**(6), pp. 860–870.
- [52] Gao, L., Yang, P., Dymond, I., Fisher, J., and Jin, Z., 2010, "Effect of Surface Texturing on the Elastohydrodynamic Lubrication Analysis of Metal-on-Metal Hip Implants," *Tribol. Int.*, **43**, pp. 1851–1860.
- [53] Gao, L. M., Meng, Q. E., Liu, F., Fisher, J., Jin, Z. M., and Hooke, C. J., 2010, "The Effect of Aspherical Geometry and Surface Texturing on the Elastohydrodynamic Lubrication of Metal-on-Metal Hip Prostheses Under Physiological Loading and Motions," *Proc. Inst. Mech. Eng. Part C J. Mech. Eng. Sci.*, **224**(12), pp. 2627–2636.
- [54] de Vicente, J., Stokes, J. R., and Spikes, H. A., 2005, "The Frictional Properties of Newtonian Fluids in Rolling—Sliding Soft-EHL Contact," *Tribol. Lett.*, **20**(3–4), pp. 273–286.
- [55] Hooke, C. J., and O'Donoghue, J. P., 1972, "Elastohydrodynamic Lubrication of Soft Highly Deformed Contacts," *J. Mech. Eng. Sci.*, **14**(1), pp. 34–48.
- [56] Adams, M. J., Briscoe, B. J., and Johnson, S. A., 2007, "Friction and Lubrication of Human Skin," *Tribol. Lett.*, **26**(3), pp. 239–253.
- [57] Jones, M. B., Fulford, G. R., Please, C. P., McElwain, D. L. S., and Collins, M. J., 2008, "Elastohydrodynamics of the Eyelid Wiper," *Bull. Math. Biol.*, **70**(2), pp. 323–343.
- [58] Stupkiewicz, S., 2009, "Finite Element Treatment of Soft Elastohydrodynamic Lubrication Problems in the Finite Deformation Regime," *Comput. Mech.*, **44**(5), pp. 605–619.
- [59] Stupkiewicz, S., Lengiewicz, J., Sadowski, P., and Kucharski, S., 2016, "Finite Deformation Effects in Soft Elastohydrodynamic Lubrication Problems," *Tribol. Int.*, **93**, pp. 511–522.
- [60] Zhao, B., Zhang, B., and Zhang, K., 2019, "Modelling Three-Dimensional Soft Elastohydrodynamic Lubrication Contact of Heterogeneous Materials," *Tribol. Int.*, **129**, pp. 377–389.
- [61] Shinkarenko, A., Kligerman, Y., and Etsion, I., 2009, "The Validity of Linear Elasticity in Analyzing Surface Texturing Effect for Elastohydrodynamic Lubrication," *ASME J. Tribol.*, **131**(2), p. 021503.
- [62] Shinkarenko, A., Kligerman, Y., and Etsion, I., 2009, "The Effect of Elastomer Surface Texturing in Soft Elasto-Hydrodynamic Lubrication," *Tribol. Lett.*, **36**(2), pp. 95–103.
- [63] Qiu, M., Chyr, A., Sanders, A. P., and Raeymaekers, B., 2014, "Designing Prosthetic Knee Joints With Bio-Inspired Bearing Surfaces," *Tribol. Int.*, **77**, pp. 106–110.
- [64] Qiu, M., and Raeymaekers, B., 2015, "The Load-Carrying Capacity and Friction Coefficient of Incompressible Textured Parallel Slider Bearings With Surface Roughness Inside the Texture Features," *Proc. Inst. Mech. Eng. Part J J. Eng. Tribol.*, **229**(4), pp. 547–556.
- [65] Venner, C. H., and Lubrecht, A. A., 2000, *Multilevel Methods in Lubrication*, Elsevier, New York.
- [66] Bergström, J. S., Kurtz, S. M., Rimnac, C. M., and Edidin, A. A., 2002, "Constitutive Modeling of Ultra-High Molecular Weight Polyethylene Under Large-Deformation and Cyclic Loading Conditions," *Biomaterials*, **23**(11), pp. 2329–2343.
- [67] Wang, F. C., and Jin, Z. M., 2005, "Elastohydrodynamic Lubrication Modeling of Artificial Hip Joints Under Steady-State Conditions," *ASME J. Tribol.*, **127**(4), pp. 729–739.
- [68] Wang, F. C., Liu, F., and Jin, Z. M., 2004, "A General Elastohydrodynamic Lubrication Analysis of Artificial Hip Joints Employing a Compliant Layered Socket Under Steady State Rotation," *Proc. Inst. Mech. Eng. Part H J. Eng. Med.*, **218**(5), pp. 283–291.
- [69] 2000, ASTM F732-17: Standard Test Method for Wear Testing of Polymeric Materials Used in Total Joint Prosthesis, ASTM International, West Conshohocken, PA.
- [70] Saikko, V., 2017, "Effect of Contact Area on the Wear and Friction of UHMWPE in Circular Translation Pin-on-Disk Tests," *ASME J. Tribol.*, **139**(6), p. 061606.
- [71] Ma, C., and Zhu, H., 2011, "An Optimum Design Model for Textured Surface with Elliptical-Shape Dimples Under Hydrodynamic Lubrication," *Tribol. Int.*, **44**, pp. 987–995.
- [72] Codrignani, A., Frohnappfel, B., Magagnato, F., Schreiber, P., Schneider, J., and Gumbsch, P., 2018, "Numerical and Experimental Investigation of Texture Shape and Position in the Macroscopic Contact," *Tribol. Int.*, **122**, pp. 46–57.
- [73] Mattei, L., Di Puccio, F., Piccigallo, B., and Ciulli, E., 2011, "Lubrication and Wear Modelling of Artificial Hip Joints: A Review," *Tribol. Int.*, **44**, pp. 532–549.
- [74] Gao, L., Dowson, D., and Hewson, R. W., 2016, "A Numerical Study of Non-Newtonian Transient Elastohydrodynamic Lubrication of Metal-on-Metal Hip Prostheses," *Tribol. Int.*, **93**, pp. 486–494.
- [75] Dobrica, M. B., Fillon, M., Pascovici, M. D., and Cicone, T., 2010, "Optimizing Surface Texture for Hydrodynamic Lubricated Contacts Using a Mass-Conserving Numerical Approach," *Proc. Inst. Mech. Eng. Part J J. Eng. Tribol.*, **224**(8), pp. 737–750.
- [76] Nečas, D., Vrbka, M., Galandáková, A., Krupka, I., and Hartl, M., 2019, "On the Observation of Lubrication Mechanisms Within Hip Joint Replacements. Part I: Hard-on-Soft Bearing Pairs," *J. Mech. Behav. Biomed. Mater.*, **89**, pp. 237–248.

- [77] Ghosh, S., Choudhury, D., Roy, T., Moradi, A., Masjuki, H. H., and Pinguan-Murphy, B., 2015, "Tribological Performance of the Biological Components of Synovial Fluid in Artificial Joint Implants," *Sci. Technol. Adv. Mater.*, **16**(4), p. 045002.
- [78] Myant, C., Underwood, R., Fan, J., and Cann, P. M., 2012, "Lubrication of Metal-on-Metal Hip Joints: The Effect of Protein Content and Load on Film Formation and Wear," *J. Mech. Behav. Biomed. Mater.*, **6**, pp. 30–40.
- [79] Stevenson, H., Jaggard, M., Akhbari, P., Vaghela, U., Gupte, C., and Cann, P., 2019, "The Role of Denatured Synovial Fluid Proteins in the Lubrication of Artificial Joints," *Biotribology*, **17**, pp. 49–63.
- [80] Qiu, Y., and Khonsari, M. M., 2009, "On the Prediction of Cavitation in Dimples Using a Mass-Conservative Algorithm," *ASME J. Tribol.*, **131**(4), p. 041702.
- [81] Ausas, R., Ragot, P., Leiva, J., Jai, M., Bayada, G., and Buscaglia, G. C., 2007, "The Impact of the Cavitation Model in the Analysis of Microtextured Lubricated Journal Bearings," *ASME J. Tribol.*, **129**(4), pp. 868–875.
- [82] Henry, Y., Bouyer, J., and Fillon, M., 2015, "An Experimental Analysis of the Hydrodynamic Contribution of Textured Thrust Bearings During Steady-State Operation: A Comparison with the Untextured Parallel Surface Configuration," *Proc. Inst. Mech. Eng. Part J J. Eng. Tribol.*, **229**(4), pp. 362–375.
- [83] Moghadam, M. N., Abdel-Sayed, P., Camine, V. M., and Pioletti, D. P., 2015, "Impact of Synovial Fluid Flow on Temperature Regulation in Knee Cartilage," *J. Biomech.*, **48**(2), pp. 370–374.
- [84] Meng, X., and Khonsari, M. M., 2018, "Viscosity Wedge Effect of Dimpled Surfaces Considering Cavitation Effect," *Tribol. Int.*, **122**, pp. 58–66.
- [85] Basri, H., Syahrom, A., Ramadhoni, T. S., Prakoso, A. T., Ammarullah, M. I., and Vincent, 2019, "The Analysis of the Dimple Arrangement of the Artificial Hip Joint to the Performance of Lubrication," *IOP Conf. Ser.: Mater. Sci. Eng.*, **620**(1), p. 012116.
- [86] Gao, L., De Boer, G., and Hewson, R., 2013, "A Multiscale Framework for Lubrication Analysis of Bearings With Textured Surface," *Advances in Structural Engineering and Mechanics*, Jeju, Korea, Sept. 8–12, pp. 959–967.